

Coexistence of Dirac Fermions and Magnons in a Layered Two-Dimensional Semiquinoid Metal-Organic Framework

Christopher Lane,^{1,2,*} Yixuan Huang,^{1,2} and Jian-Xin Zhu^{1,2}

¹*Theoretical Division, Los Alamos National Laboratory, Los Alamos, New Mexico 87545, USA*

²*Center for Integrated Nanotechnologies, Los Alamos National Laboratory, Los Alamos, New Mexico 87545, USA*

(Dated: October 3, 2023)

We predict the magnetic and electronic properties of a novel metal-organic framework. By combining density functional theory and density matrix renormalization group approaches, we find the diatomic Kagome crystal structure of the metal-semiquinoid framework $(\text{H}_2\text{NMe}_2)_2\text{M}_2(\text{Cl}_2\text{dhhq})_3$ ($\text{M} = \text{Ti}, \text{V}, \text{Cr}, \text{Mn}, \text{Fe}, \text{Co}, \text{Ni}, \text{Cu}, \text{and Zn}$) to host a rich variety of antiferromagnetic (AFM) and ferromagnetic (FM) Dirac semimetallic, spin-polarized Dirac fermions, and flat band magnetic insulators and metallic phases. Concomitantly, the spin excitation spectrum of the various magnetic systems display multiple Dirac-like and nodal-ring crossings. This suggests that the metal-semiquinoid system is an ideal platform for examining the intertwining of Dirac fermions and magnons.

INTRODUCTION

Low-dimensional magnetism lies at the heart of numerous novel phenomena in condensed matter physics, including high- T_c superconductivity [1], topological quantum spin liquids [2], non-Fermi liquid behavior [3], and quantum criticality [4]. In simple isotropic spin systems with short-range exchange interactions, long-range magnetic order is predicted to be forbidden in one- and two-dimensions due to strong thermal fluctuations [5, 6]. However, in real crystalline materials, the spherical atomic symmetry of the magnetic ions is reduced by the local chemical environment. This suggests a straightforward tuning of the magnetic anisotropy can reduce or strengthen spin fluctuations and thus control various forms of magnetic order. Accordingly, the central task in characterizing and designing quantum magnets becomes understanding and manipulating the delicate interplay between spin and orbital motions of an electron, and their coupling to the lattice.

The recent discovery of two-dimensional (2D) van der Waals magnets presents a unique opportunity to study the fundamental processes governing the emergence of magnetic correlations and ordering under 2D confinement, and advance application in spintronics and quantum information sciences [7–13]. Due to their reduced dimensionality, 2D magnets are an ideal play ground for observing topological superconductivity [13] and frustrated quantum magnetism, such as resonating valence bonds [14] and 2D Kitaev spin liquids [15], which gives us access to fractionalized charge states of matter and new elementary excitations such as Majorana fermions [16–19]. However, to date these exotic states have yet to be observed, despite a number of theoretical predictions [20–23]

Crucial to the discovery of novel magnetic states and the design of next generation microelectronics is the control and manipulation of the magnetic properties. To this end, a number of approaches have been fruitful in cou-

pling key parameters governing the underlying electronic structure to external perturbations such as strain, light, gating, proximity and moiré heterostructuring [24]. For example, interlayer interactions in Fe_3GeTe_2 thin-films drive a crossover from a single FM domain to an inhomogeneous labyrinthine domain phase with increased thickness. This transition is accompanied by a fast increase in the Curie temperature from 130 K to 207 K for just five layers [25]. Similarly, when two monolayer sheets of CrI_3 are twisted with respect to one another, the resulting moiré pattern promotes islands of AFM and FM interlayer coupled domains following the moiré pattern [26]. Finally, by electrostatic doping and optical pumping, the magnetization, Curie temperature, and polarization of the magnetic state can be directly controlled and fine-tuned [27, 28]. Despite these significant advances, many of these external perturbations are hard to implement within a realistic environment. Therefore, to be able to incorporate 2D magnetic materials into microcircuitry, we must design the *intrinsic* properties of the magnetic thin-films themselves.

Metal-organic frameworks (MOFs) offer a new route to overcome these challenges to build new magnetic materials with high synthetic programmability and tunability. MOFs consist of metal ions coordinated to organic ‘linker’ ligands to form one-, two-, or three-dimensional structures. So far, significant attention has been concentrated on the porosity and chemical stability of MOFs in connection with applications in gas separation and storage, and catalysis [29]. However, recently MOFs have been recognized as an ideal platform materials with desired magnetic and electronic properties [30, 31]. 2D MOFs in particular, have been proposed [32] to host a rich variety of electronic band structure, e.g. Dirac cones and topological flat-bands, and a range of magnetic orders. Despite these intriguing properties, a limited number of compounds with long-range order have been predicted and synthesized.

In this Article, we predict the magnetic and elec-

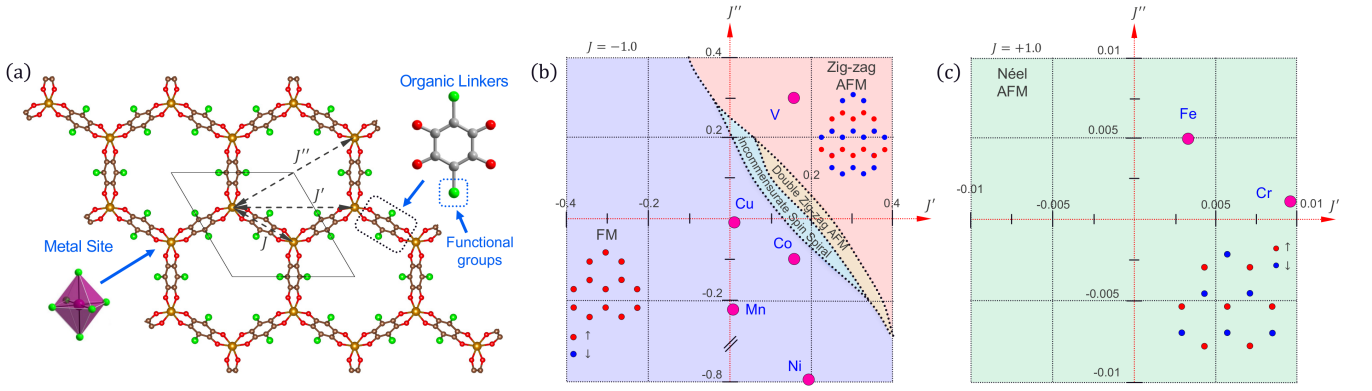


FIG. 1. (color online) (a) Crystal structure of the metal-semiquinoid framework $(\text{H}_2\text{NMe}_2)_2\text{M}_2(\text{Cl}_2\text{dhbq})_3$, with the transition-metal, oxygen, carbon, and chlorine shown as gold, red, grey, and green spheres. The first-nearest (J), second-nearest (J'), and third-nearest (J'') neighbor exchange parameters are indicated on the honeycomb lattice of transition-metal sites within a 2×2 super cell of the metal-semiquinoid framework. The black lines mark the unit cell. (b) and (c) shows the normalized J , J' , and J'' exchange parameters for all $3d$ transition metals with $J < 0$ and $J > 0$, respectively, overlaid on the phase diagram determined with $\langle S \rangle = 1$.

tronic properties of the metal-semiquinoid framework $(\text{H}_2\text{NMe}_2)_2\text{M}_2(\text{Cl}_2\text{dhbq})_3$ ($\text{dhbq}^{n-} = \text{deprotonated 2,5-dihydroxybenzoquinone}$) for all $3d$ transition-metals ($M = \text{Ti, V, Cr, Mn, Fe, Co, Ni, Cu, and Zn}$). We find this metal-semiquinoid framework to display a diverse array of magnetic and electronic properties under different transition-metal substitutions. Specifically, long range FM, Néel, and Zig-zag AFM magnetic orders are found to be robust within the diatomic Kagome crystal structure. Additionally, the crystal structure in combination with the magnetic state yields a variety of band topologies including AFM and FM Dirac semimetals, spin-polarized Dirac fermions, and flat band magnetic insulators and metals. We calculate magnetic excitation spectrum of each system and find it clearly exhibit multiple Dirac crossings in the FM and zig-zag AFM compounds. Furthermore, multiple compounds studied display the coexistence of Dirac fermions and magnons.

RESULTS AND DISCUSSION

Magnetic and Electronic Ground State

Figure 1 (a) shows the primitive unit cell of the $[\text{M}_2\text{L}_3]^{2-}$ MOF along the c -axis, where the MO_6 octahedra if the six oxygen sites are in plane, a use of octahedra is appropriate? They are not in the plane, it only appears so looking along the c -axis. Maybe we add a side view in the SM. form a 2D honeycomb lattice and the semiquinoid linkers connect the edges of the nearest-neighbor octahedra. The H_2NMe_2 and H_2O molecules have been neglected for simplicity. In order to determine the exchange coupling strength between neighboring transition-metals, we map the total energies of the

various spin configurations γ onto those of the third-nearest-neighbor Heisenberg Hamiltonian [33], written as

$$\mathcal{H} = \sum_{\langle i < j \rangle} J_{ij} \mathbf{S}_i \cdot \mathbf{S}_j + \sum_{\langle\langle i < j \rangle\rangle} J'_{ij} \mathbf{S}_i \cdot \mathbf{S}_j + \sum_{\langle\langle\langle i < j \rangle\rangle\rangle} J''_{ij} \mathbf{S}_i \cdot \mathbf{S}_j. \quad (1)$$

Here $i(j)$ indexes the magnetic ion lattice positions, \mathbf{S}_i is the local magnetic moment on lattice site i . J_{ij} , J'_{ij} , and J''_{ij} denote the nearest-neighbor, next-nearest-neighbor, and third-nearest-neighbor exchange interaction strength, with the symmetry properties of $J_{ij}^{(i,')} = J_{ji}^{(i,')}$. Assuming a fully isotropic bond independent model, 2^4 unique spin configurations are needed to fully determine $J^{i, \dots, i'}$. By summing configurations γ and $-\gamma$, and using the resulting eight equations to solve for J , J' , and J'' , we find

$$J = \frac{(E^1 + E^4 + E^5 + E^6) - (E^2 + E^3 + E^7 + E^8)}{16 \cdot 3 \langle S \rangle^2}, \quad (2a)$$

$$J' = \frac{(E^1 + E^3 + E^5 + E^7) - (E^2 + E^4 + E^6 + E^8)}{16 \cdot 6 \langle S \rangle^2}, \quad (2b)$$

$$J'' = \frac{(E^1 + E^3 + E^4 + E^8) - (E^2 + E^5 + E^6 + E^7)}{16 \cdot 3 \langle S \rangle^2}, \quad (2c)$$

where,

$$\begin{aligned} E^1 &= E^{++++} + E^{----}, & E^5 &= E^{+++} + E^{---}, \\ E^2 &= E^{-+++} + E^{+---}, & E^6 &= E^{++--} + E^{--++}, \\ E^3 &= E^{+-++} + E^{-+-}, & E^7 &= E^{+--+} + E^{-+-}, \\ E^4 &= E^{++--} + E^{--+-}, & E^8 &= E^{+--+} + E^{-+-}. \end{aligned}$$

Here, each spin configuration γ is given by the direction of the magnetic moment on each successive nearest-neighbor ring, e.g., $+-+-$. In calculating the total energies, we found $E^\gamma \approx E^{-\gamma}$, thereby allowing us to reduce the number of *ab initio* calculations by half.

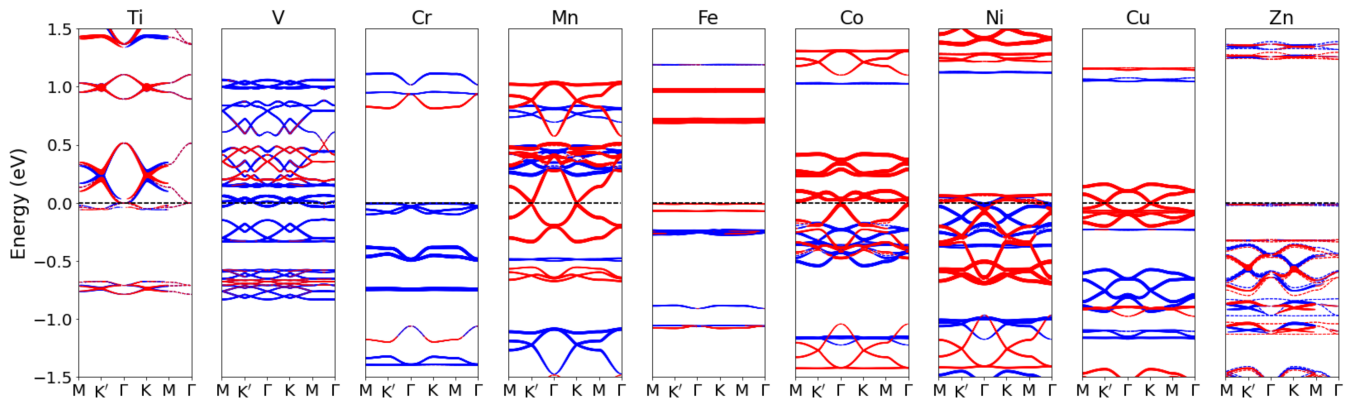


FIG. 2. (color online) Spin-resolved electronic band dispersions with (dots) and without (dashed line) spin-orbit coupling of the metal-semiquinoid framework $(\text{H}_2\text{NMe}_2)_2\text{M}_2(\text{Cl}_2\text{dhbq})_3$ for various $3d$ transition-metals. The sizes of the dots are proportional to the spin-polarization $\langle S_z \rangle$, with the spin-up (down) states indicated in red (blue) color.

Figure 1 (b) and (c) present the normalized first-, second-, and third-nearest neighbor exchange parameters for all $3d$ transition metals. Ti and Zn display negligible and zero magnetic polarization on the atomic sites, respectively, yielding no exchange parameters. For transition-metals to the left of Co on the periodic table, J and J'' alternate between positive and negative values, whereas Co, Ni, and Cu are consistently negative. The next-nearest neighbor exchange coupling is found to be finite, despite the 15.66 \AA separation, and positive for all magnetic ions. Interestingly, this oscillatory behavior in the sign of the exchange coupling indicates a possible sensitive dependence of the ground state magnetic order on the d -electron count. For the value of the exchange parameters in energy units, see the Supplementary Materials [34].

The magnetic ground state is obtained for each transition-metal within the DMRG, along with the resulting phase diagram for Eq. (1) overlaid in panels (b) and (c) of Fig. 1. Note the indicated phase boundaries are for the various transition-metals with $\langle S \rangle = 1$ and cannot facilitate direct comparison between species since $\langle S \rangle$ is not necessarily equivalent. Vanadium exhibits a zig-zag AFM ground state in close proximity to a double zig-zag, incommensurate spin spiral, and FM phase transition. The zig-zag AFM, FM [35–37], and double zig-zag [37] phases are also found in similar studies for $\langle S \rangle = 1/2$, but the incommensurate spin spiral phase is absent due to enhanced quantum fluctuations for smaller $\langle S \rangle$. As the atomic number increases, the ground state alternates between FM and Néel-type AFM order up through Fe. For Co, Ni, and Cu the ground state settles into a robust FM order.

Structurally, $[\text{M}_2\text{L}_3]^{2-}$ may be mapped onto the diatomic kagome lattice resulting from the $\sim 90^\circ$ dihedral angles between the organic ligands [38]. This geometry is predicted to produce two sets of enantiomorphic Yin-Yang kagome bands with a Dirac crossing at $K(K')$ in the

Brillouin zone. When spin-orbit coupling is included a finite non-trivial gap appears at the Dirac nodes, thereby transforming the system from a topological semimetal to a topological insulator with two flat bands of opposite spin Chern numbers [32]. Such diatomic kagome crystals have been proposed as a platform for a triplet excitonic insulator state [39] and to host novel quantum Hall effects [40].

Figure 2 shows the spin-resolved electronic band dispersion for each $[\text{M}_2\text{L}_3]^{2-}$ in its associated magnetic ground state. Compared to idealized tight-binding models [32], a rich variety of electronic structures are exhibited showing a sensitive dependence on magnetic ground state and d -electron count. Specifically, Cr, Fe, and Zn display an AFM and a NM insulating state, respectively, with highly localized carriers as demonstrated by the extremely flat bands at the valence band edges, similar to those in kagome and magic-angle twisted bilayer graphene [41].

Mn and Cu host fully spin-polarized Dirac fermions at the Fermi level that are clearly separated from other bands in the system by $\sim 250 \text{ meV}$. Interestingly, the bandwidth and Fermi velocity of the linearly dispersing states of the Cu-based compound are significantly reduced compared to those in Mn, indicating an enhancement in the electron–electron interaction strength. Many theoretical studies suggest that Dirac materials with strong electron–electron interactions may host an excitonic insulator ground state [42–44], however, such a phase has yet to be observed in a Dirac material. In contrast, FM Ni is a metal and FM Co is a narrow indirect band gap ($\sim 25 \text{ meV}$) FM semiconductor. Finally, under electron doping V and Ti are in close proximity to a AFM Dirac semimetal and the elusive nearly nonmagnetic spin–valley coupled Dirac semimetal phase, respectively.

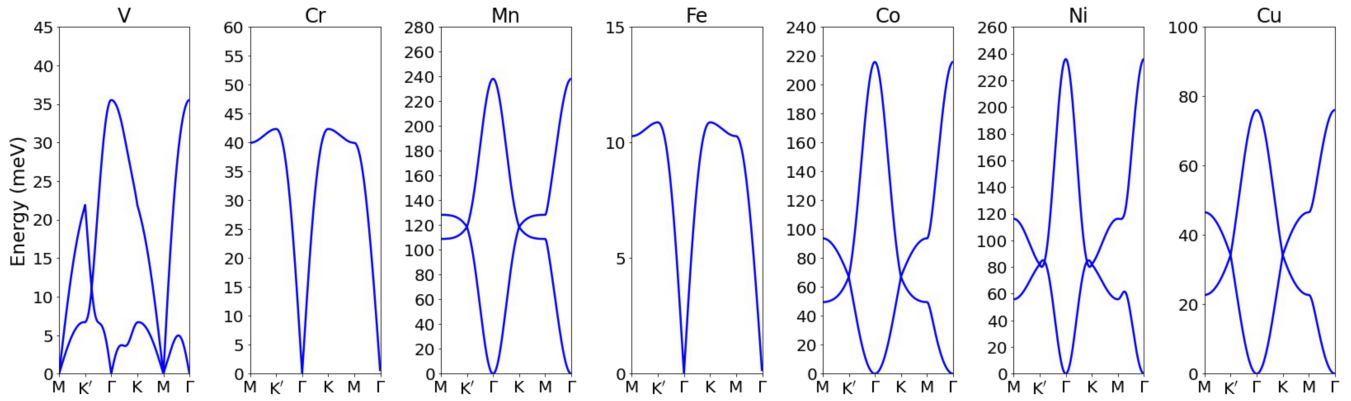


FIG. 3. (color online) Magnon excitation spectrum of the metal-semiquinoid framework $(\text{H}_2\text{NMe}_2)_2\text{M}_2(\text{Cl}_2\text{dmbq})_3$ for various $3d$ transition-metals.

Magnon Excitation Spectrum

We now consider the elementary excitations of the FM, Néel AFM and zig-zag AFM phases. To derive their dispersion relations, we map the spin operators in the Heisenberg model, Eq. (1), onto a set of boson creation

(annihilation) operators through the Holstein-Primakoff transformation [45, 46]. By retaining the lowest-order terms, the dynamical matrix is diagonalized by employing a Bogoliubov canonical transformation [47] (see the Supplementary Materials for details [34]), which yields the magnon energy dispersion

$$\varepsilon_{\text{FM}}^{\pm}(\mathbf{k}) = S(J''\gamma_{\mathbf{k}}^{(2)} - 3J' - 6J'' - 3J''') \pm S|J'\gamma_{\mathbf{k}}^{(1)} + J'''\gamma_{\mathbf{k}}^{(3)}|, \quad (3)$$

$$\varepsilon_{\text{Néel}}(\mathbf{k}) = S\sqrt{(J''\gamma_{\mathbf{k}}^{(2)} + 3J' - 6J'' + 3J''')^2 - |J'\gamma_{\mathbf{k}}^{(1)} + J'''\gamma_{\mathbf{k}}^{(3)}|^2}, \quad (4)$$

$$\varepsilon_{\text{zig-zag}}^{\pm}(\mathbf{k}) = S\sqrt{\chi_1^2 + |\phi_1|^2 - \chi_2^2 - |\phi_2|^2 \pm 2\sqrt{(\chi_1\Im\phi_1 + \chi_2\Im\phi_2)^2 + (\chi_1\Re\phi_1 - \chi_2\Re\phi_2)^2} - (\Im\phi_1\Re\phi_2 + \Im\phi_2\Re\phi_1)^2}, \quad (5)$$

where χ_1 , χ_2 , ϕ_1 , ϕ_2 , and $\gamma_{\mathbf{k}}^{(1)}, \dots, \gamma_{\mathbf{k}}^{(3)}$ are functions of \mathbf{k} and $J^{i\dots i}$; see their expressions in the Supplementary Materials [34].

Figure 3 presents the magnon dispersion for each $3d$ transition metal. In Cr and Fe based semiquinoid metal-organic frameworks a single magnon band is found that follows a linear dispersion to zero at Γ , as is typical for antiferromagnets. The FM Mn, Co, and Cu based compounds display clear Dirac crossings at K (K'), along with the standard quadratic band dispersion at Γ . Ni exhibits a Dirac magnon nodal loop encircling the K (K') point in the Brillouin zone, similar to that proposed in the honeycomb chromium halide compounds [48]. Finally, the the zig-zag AFM state of V produces a very sharp Dirac crossing near K' and two linearly dispersing bands at M due to the finite ordering vector of the underlying magnetic order.

Dirac fermions display a wide range of unique properties including large opacity, huge charge carrier mobility and the anomalous quantum Hall effect [49, 50]. Similarly, magnetic systems have been predicted and observed

to host Dirac magnons [51–53], exhibiting gapped bands with non-trivial Chern numbers [7], surface states [53], and a magnon thermal Hall effect [54]. Here, we find the $[\text{M}_2\text{L}_3]^{2-}$ MOF composed of V, Mn, Co, Ni, and Cu to display the coexistence of Dirac fermions and magnons which allows for the intertwining of non-trivial fermionic and bosonic band topologies. Consequently, by combining dissipationless long distance magnon and charge propagation, this family of materials could provide a path towards charge-magnetic coupled multifunctional magnonic and spintronic devices.

CONCLUSIONS

We have shown the semiquinoid-based metal-organic framework $(\text{H}_2\text{NMe}_2)_2\text{M}_2(\text{Cl}_2\text{dmbq})_3$ to host a rich landscape of electronic and magnetic properties for $3d$ transition-metals. In particular, multiple compounds demonstrate the coexistence of Dirac fermions and magnons, which hold promise is dissipationless charge

and spin transport and unique non-trivial fermion-magnon coupled band topologies. Moreover, the inclusion of higher order corrections, e.g., ring exchange [55], can open a magnon gap [56] and give rise to possible spin liquid phases [57].

METHODS

First-Principles Calculations

Ab initio calculations were carried out using the pseudopotential projector-augmented wave method [58] implemented in the Vienna *ab initio* simulation package (VASP) [59, 60] with an energy cutoff of 400 eV for the plane-wave basis set. Exchange-correlation effects were treated using the Perdew-Burke-Ernzerhof (PBE) GGA density functional [61], where a $7 \times 7 \times 11$ Γ -centered k-point mesh was used to sample the Brillouin zone of the primitive cell. We used the pristine MOF structure as determined by Jeon *et al.* [62] with the inert solvents removed. A total energy tolerance of 10^{-6} eV was used as the convergence criteria on the self-consistent charge density.

Infinite Density Matrix Renormalization Group Calculations

The magnetic ground state of the effective Heisenberg Hamiltonian was determined by applying the infinite density matrix renormalization group (DMRG) [63–65] approach with $U(1)$ spin symmetry on cylinders with open boundary condition along the axial direction and periodic boundary conditions for the circumferential direction. Results on cylinders of width 6 and 8 unit cells are found to be consistent for each transition metal, where up to 5000 bond dimensions were used to obtain a truncation error of 10^{-5} . The truncation error is defined as the sum of the discarded reduced density matrix eigenvalues during sweeps. Simulations were performed using the TeNPy library (version 0.9.0) [66].

DATA AVAILABILITY

All data supporting the findings of this study are available from the corresponding author upon a reasonable request.

REFERENCES

* laneca@lanl.gov

[1] Fradkin, E., Kivelson, S. A. & Tranquada, J. M. Colloquium: Theory of intertwined orders in high temperature superconductors. *Reviews of Modern Physics* **87**, 457 (2015).

[2] Zhou, Y., Kanoda, K. & Ng, T.-K. Quantum spin liquid states. *Reviews of Modern Physics* **89**, 025003 (2017).

[3] Stewart, G. Non-fermi-liquid behavior in d- and f-electron metals. *Reviews of Modern Physics* **73**, 797 (2001).

[4] Sachdev, S. Quantum magnetism and criticality. *Nature Physics* **4**, 173–185 (2008).

[5] Hohenberg, P. C. Existence of long-range order in one and two dimensions. *Physical Review* **158**, 383 (1967).

[6] Mermin, N. D. & Wagner, H. Absence of ferromagnetism or antiferromagnetism in one-or two-dimensional isotropic heisenberg models. *Physical Review Letters* **17**, 1133 (1966).

[7] Zhu, F. *et al.* Topological magnon insulators in two-dimensional van der Waals ferromagnets CrSiTe₃ and CrGeTe₃: Toward intrinsic gap-tunability. *Science Advances* **7**, eabi7532 (2021).

[8] Gong, C. *et al.* Discovery of intrinsic ferromagnetism in two-dimensional van der Waals crystals. *Nature* **546**, 265–269 (2017).

[9] Huang, B. *et al.* Layer-dependent ferromagnetism in a van der Waals crystal down to the monolayer limit. *Nature* **546**, 270–273 (2017).

[10] Kim, K. *et al.* Large anomalous Hall current induced by topological nodal lines in a ferromagnetic van der Waals semimetal. *Nature Materials* **17**, 794–799 (2018).

[11] Kim, S. Y. *et al.* Charge-spin correlation in van der Waals antiferromagnet NiPS₃. *Physical Review Letters* **120**, 136402 (2018).

[12] Bonilla, M. *et al.* Strong room-temperature ferromagnetism in VSe₂ monolayers on van der Waals substrates. *Nature Nanotechnology* **13**, 289–293 (2018).

[13] Li, Y. *et al.* Electronic properties of the bulk and surface states of Fe_{1+y}Te_{1-x}Se_x. *Nature Materials* **20**, 1221–1227 (2021).

[14] Anderson, P. W. Resonating valence bonds: A new kind of insulator? *Materials Research Bulletin* **8**, 153–160 (1973).

[15] Kitaev, A. Anyons in an exactly solved model and beyond. *Annals of Physics* **321**, 2–111 (2006).

[16] Huang, Y. & Sheng, D. Topological chiral and nematic superconductivity by doping mott insulators on triangular lattice. *Physical Review X* **12**, 031009 (2022).

[17] Balents, L. Spin liquids in frustrated magnets. *Nature* **464**, 199–208 (2010).

[18] Savary, L. & Balents, L. Quantum spin liquids: a review. *Reports on Progress in Physics* **80**, 016502 (2016).

[19] Knolle, J. & Moessner, R. A field guide to spin liquids. *Annual Review of Condensed Matter Physics* **10**, 451–472 (2019).

[20] Xu, C. *et al.* Possible Kitaev quantum spin liquid state in 2d materials with $s = 3/2$. *Physical Review Letters* **124**, 087205 (2020).

[21] Ji, J. *et al.* Rare-earth chalcogenides: A family of van der Waals layered Kitaev spin liquid candidates. *Chinese Physics Letters* **38**, 047502 (2021).

[22] Loidl, A., Lunkenheimer, P. & Tsurkan, V. On the proximate Kitaev quantum-spin liquid α -RuCl₃: thermodynamics, excitations and continua. *Journal of Physics: Condensed Matter* (2021).

[23] Takagi, H., Takayama, T., Jackeli, G., Khaliullin, G. & Nagler, S. E. Concept and realization of Kitaev quantum spin liquids. *Nature Reviews Physics* **1**, 264–280 (2019).

- [24] Burch, K. S., Mandrus, D. & Park, J.-G. Magnetism in two-dimensional van der Waals materials. *Nature* **563**, 47–52 (2018).
- [25] Fei, Z. *et al.* Two-dimensional itinerant ferromagnetism in atomically thin Fe₃GeTe₂. *Nature Materials* **17**, 778–782 (2018).
- [26] Xu, Y. *et al.* Coexisting ferromagnetic–antiferromagnetic state in twisted bilayer CrI₃. *Nature Nanotechnology* **17**, 143–147 (2022).
- [27] Jiang, S., Li, L., Wang, Z., Mak, K. F. & Shan, J. Controlling magnetism in 2D CrI₃ by electrostatic doping. *Nature Nanotechnology* **13**, 549–553 (2018).
- [28] Afanasiev, D. *et al.* Controlling the anisotropy of a van der Waals antiferromagnet with light. *Science Advances* **7**, eabf3096 (2021).
- [29] Wang, Q. & Astruc, D. State of the art and prospects in metal–organic framework (MOF)-based and MOF-derived nanocatalysis. *Chemical Reviews* **120**, 1438–1511 (2019).
- [30] Yamada, M. G., Fujita, H. & Oshikawa, M. Designing Kitaev spin liquids in metal-organic frameworks. *Physical Review Letters* **119**, 057202 (2017).
- [31] Murphy, R. A. *et al.* Exchange bias in a layered metal–organic topological spin glass. *ACS central science* **7**, 1317–1326 (2021).
- [32] Jiang, W., Ni, X. & Liu, F. Exotic topological bands and quantum states in metal–organic and covalent–organic frameworks. *Accounts of Chemical Research* **54**, 416–426 (2021).
- [33] Xiang, H., Lee, C., Koo, H.-J., Gong, X. & Whangbo, M.-H. Magnetic properties and energy-mapping analysis. *Dalton Transactions* **42**, 823–853 (2013).
- [34] See Supplemental Materials at [URL will be inserted by publisher] for more details.
- [35] Watanabe, Y., Trebst, S. & Hickey, C. Frustrated ferromagnetism of honeycomb Cobaltates: Incommensurate spirals, quantum disordered phases, and out-of-plane ising order. *arXiv preprint arXiv:2212.14053* (2022).
- [36] Bose, A. *et al.* Proximate dirac spin liquid in the J_1 - J_3 xxz model for honeycomb cobaltates. *arXiv preprint arXiv:2212.13271* (2022).
- [37] Jiang, S., White, S. R. & Chernyshev, A. Quantum phases in the honeycomb-lattice J_1 - J_3 ferro-antiferromagnetic model. *arXiv preprint arXiv:2304.06062* (2023).
- [38] Ni, X., Zhou, Y., Sethi, G. & Liu, F. π -orbital yin–yang kagome bands in anilato-based metal–organic frameworks. *Physical Chemistry Chemical Physics* **22**, 25827–25832 (2020).
- [39] Sethi, G., Zhou, Y., Zhu, L., Yang, L. & Liu, F. Flat-band-enabled triplet excitonic insulator in a diatomic kagome lattice. *Physical Review Letters* **126**, 196403 (2021).
- [40] Zhou, Y., Sethi, G., Liu, H., Wang, Z. & Liu, F. Excited quantum Hall effect: enantiomorphic flat bands in a Yin–Yang kagome lattice. *arXiv preprint arXiv:1908.03689* (2019).
- [41] Cao, Y. *et al.* Correlated insulator behaviour at half-filling in magic-angle graphene superlattices. *Nature* **556**, 80–84 (2018).
- [42] Pertsova, A. & Balatsky, A. V. Dynamically induced excitonic instability in pumped dirac materials. *Annalen der Physik* **532**, 1900549 (2020).
- [43] Kotov, V. N., Uchoa, B., Pereira, V. M., Guinea, F. & Neto, A. C. Electron-electron interactions in graphene: Current status and perspectives. *Reviews of modern physics* **84**, 1067 (2012).
- [44] Drut, J. E. & Lähde, T. A. Is graphene in vacuum an insulator? *Physical review letters* **102**, 026802 (2009).
- [45] Holstein, T. & Primakoff, H. Field dependence of the intrinsic domain magnetization of a ferromagnet. *Physical Review* **58**, 1098 (1940).
- [46] Khomskii, D. I. *Basic aspects of the quantum theory of solids: order and elementary excitations* (Cambridge university press, 2010).
- [47] We note that in contrast to the Fermi systems where the dynamical excitation matrix is identical to the Hamiltonian coefficient matrix, the dynamic matrix is distinct in the case of Bose systems [67]. Therefore care must be taken when calculating the magnon excitation spectrum.
- [48] Owerre, S. Dirac magnon nodal loops in quasi-2d quantum magnets. *Scientific reports* **7**, 6931 (2017).
- [49] Novoselov, K. Nobel lecture: Graphene: Materials in the flatland. *Reviews of modern physics* **83**, 837 (2011).
- [50] Neto, A. C., Guinea, F., Peres, N. M., Novoselov, K. S. & Geim, A. K. The electronic properties of graphene. *Reviews of modern physics* **81**, 109 (2009).
- [51] Fransson, J., Black-Schaffer, A. M. & Balatsky, A. V. Magnon dirac materials. *Physical Review B* **94**, 075401 (2016).
- [52] Owerre, S. A first theoretical realization of honeycomb topological magnon insulator. *Journal of Physics: Condensed Matter* **28**, 386001 (2016).
- [53] Pershoguba, S. S. *et al.* Dirac magnons in honeycomb ferromagnets. *Physical Review X* **8**, 011010 (2018).
- [54] Onose, Y. *et al.* Observation of the magnon hall effect. *Science* **329**, 297–299 (2010).
- [55] Coldea, R. *et al.* Spin waves and electronic interactions in La₂CuO₄. *Physical Review Letters* **86**, 5377 (2001).
- [56] Li, Y. *et al.* Ring-exchange interaction effects on magnons in Dirac magnet CoTiO₃. *arXiv preprint arXiv:2212.05278* (2022).
- [57] Cookmeyer, T., Motruk, J. & Moore, J. E. Four-spin terms and the origin of the chiral spin liquid in Mott insulators on the triangular lattice. *Physical Review Letters* **127**, 087201 (2021).
- [58] Kresse, G. & Joubert, D. From ultrasoft pseudopotentials to the projector augmented-wave method. *Phys. Rev. B* **59**, 1758–1775 (1999).
- [59] Kresse, G. & Furthmüller, J. Efficient iterative schemes for ab initio total-energy calculations using a plane-wave basis set. *Phys. Rev. B* **54**, 11169–11186 (1996).
- [60] Kresse, G. & Hafner, J. Ab initio molecular dynamics for open-shell transition metals. *Phys. Rev. B* **48**, 13115–13118 (1993).
- [61] Perdew, J. P., Burke, K. & Ernzerhof, M. Generalized gradient approximation made simple. *Physical Review Letters* **77**, 3865 (1996).
- [62] Jeon, I.-R., Negru, B., Van Duyne, R. P. & Harris, T. D. A 2D semiquinone radical-containing microporous magnet with solvent-induced switching from T_c = 26 to 80 K. *Journal of the American Chemical Society* **137**, 15699–15702 (2015).
- [63] White, S. R. Density matrix formulation for quantum renormalization groups. *Physical Review Letters* **69**, 2863 (1992).

- [64] White, S. R. Density-matrix algorithms for quantum renormalization groups. *Physical Review B* **48**, 10345 (1993).
- [65] Schollwöck, U. The density-matrix renormalization group in the age of matrix product states. *Annals of physics* **326**, 96–192 (2011).
- [66] Hauschild, J. & Pollmann, F. Efficient numerical simulations with tensor networks: Tensor network python (tenpy). *SciPost Physics Lecture Notes* 005 (2018).
- [67] Xiao, M.-W. Theory of transformation for the diagonalization of quadratic Hamiltonians. *arXiv preprint arXiv:0908.0787* (2009).

We thank Jennifer Hollingsworth and Ekaterina Dogoplova for useful discussions. This work was carried out under the auspices of the U.S. Department of Energy (DOE) National Nuclear Security Administration (NNSA) under Contract No. 89233218CNA000001. It was supported by the LDRD program (C.L.), Center for Integrated Nanotechnologies (Y.H.), a DOE BES user facility, in partnership with the LANL Institutional Computing Program for computational resources, and Quantum Science Center (J.-X.Z.), a U.S. DOE Office of

Science Quantum Information Science Research Center. Additional computations were performed at the National Energy Research Scientific Computing Center (NERSC), a U.S. Department of Energy Office of Science User Facility located at Lawrence Berkeley National Laboratory, operated under Contract No. DE-AC02-05CH11231 using NERSC award ERCAP0020494.

AUTHOR CONTRIBUTIONS

C.L. and Y.H. performed computations and C.L., Y.H., and J.Z. analyzed the data. C.L., and J.Z. led the investigations, designed the computational approaches, and J.Z. provided computational infrastructure. All authors contributed to the writing of the manuscript.

COMPETING INTERESTS

The authors declare no competing interests.

–Supplementary Materials–
**Coexistence of Dirac Fermions and Magnons in a Layered Two-Dimensional
 Semiquinoid Metal-Organic Framework**

Christopher Lane,^{1,2,*} Yixuan Huang,^{1,2} and Jian-Xin Zhu^{1,2}

¹*Theoretical Division, Los Alamos National Laboratory, Los Alamos, New Mexico 87545, USA*

²*Center for Integrated Nanotechnologies, Los Alamos National Laboratory, Los Alamos, New Mexico 87545, USA*

(Dated: October 3, 2023)

S1. MAGNETIC EXCHANGE PARAMETERS

In order to determine the strength of the exchange coupling between neighboring transition-metals in the $[\text{M}_2\text{L}_3]^{2-}$ MOF, we map the total energies of the various spin configurations onto those of the third-nearest-neighbor Heisenberg Hamiltonian in the mean-field approximation 1. Figure S1 shows a 2×2 super cell of the $[\text{M}_2\text{L}_3]^{2-}$ MOF with the color of the transition-metal sites marking the central magnetic ion (blue dot), nearest-neighbors (yellow dot), next-nearest-neighbors (green dot), and next-next-nearest-neighbors (red dot). For this crystal lattice, we can write the Heisenberg spin Hamiltonian as,

$$\mathcal{H} = \sum_{\langle i < j \rangle} J_{ij} S_i S_j + \sum_{\langle\langle i < j \rangle\rangle} J'_{ij} S_i S_j + \sum_{\langle\langle\langle i < j \rangle\rangle\rangle} J''_{ij} S_i S_j, \quad (1)$$

where $i(j)$ indexes the magnetic ion lattice positions, S_i is the local magnetic moment on lattice site i , J_{ij} , J'_{ij} , and J''_{ij} denote the nearest-neighbor, next-nearest-neighbor, and third-nearest-neighbor exchange interaction strength between sites i and j such that $J_{ij}^{(t'')} = J_{ji}^{(t'')}$. Furthermore, the number of magnetic configurations needed to fully determine the exchange parameters is reduced by assuming J_{ij} to be bond independent. This allows us to re-label the various terms in the Hamiltonian by nearest-neighbor rings a , b , c , and d , yielding,

$$\mathcal{H} = 3J S_a S_b + 6J' S_a S_c + 3J'' S_a S_d, \quad (2)$$

where the leading integer coefficient is the coordination number for each ring of neighbors.

Since the local magnetic moment on each site can be either $+$ or $-$, there are $2^4 = 16$ unique spin configurations that may be realized. Each configuration γ is given by the direction of each moment for each successive nearest-neighbor ring, e.g., $+-+-$ meaning $\langle S_a \rangle, \langle S_c \rangle > 0$ and $\langle S_b \rangle, \langle S_d \rangle < 0$. Additionally, since the total energy of configurations γ and $-\gamma$ are degenerate, the number of *ab initio* calculations is reduced by half. Finally, by summing configurations γ and $-\gamma$ and using the resulting

	J (meV)	J' (meV)	J'' (meV)	J_{\perp} (meV)	S
Ti	–	–	–	–	0.0
V	-7.8704	1.2844	2.4126	-1.1097E-02	1
Cr	9.6971	9.91E-02	1.11E-02	-2.9555E-04	1.5
Mn	-21.4668	3.90E-02	-4.9882	-3.2499E-04	1.5
Fe	1.8228	6.55E-03	9.01E-03	8.52187E-04	2
Co	-21.6576	3.0208	-2.3148	-3.6692E-02	1.5
Ni	-21.9392	3.9891	-17.3706	-0.88693	1
Cu	-24.9644	0.8441	-0.3804	-2.7028	0.5
Zn	–	–	–	–	0.0

TABLE S1. Intra- and inter-planar exchange parameters and spin magnitude in the metal-semiquinoid framework $(\text{H}_2\text{NMe}_2)_2\text{M}_2(\text{Cl}_2\text{dmbq})_3$ for all 3d transition-metals.

eight equations to solve for J , J' , and J'' , we find

$$J = \frac{(E^1 + E^4 + E^5 + E^6) - (E^2 + E^3 + E^7 + E^8)}{16 \cdot 3 \langle S \rangle^2}, \quad (3)$$

$$J' = \frac{(E^1 + E^3 + E^5 + E^7) - (E^2 + E^4 + E^6 + E^8)}{16 \cdot 6 \langle S \rangle^2}, \quad (4)$$

$$J'' = \frac{(E^1 + E^3 + E^4 + E^8) - (E^2 + E^5 + E^6 + E^7)}{16 \cdot 3 \langle S \rangle^2}, \quad (5)$$

where we have defined,

$$\begin{aligned} E^1 &= E^{++++} + E^{----}, & E^5 &= E^{+++-} + E^{----}, \\ E^2 &= E^{-+++} + E^{+---}, & E^6 &= E^{++--} + E^{--++}, \\ E^3 &= E^{+-++} + E^{-+--}, & E^7 &= E^{+--+} + E^{-+++}, \\ E^4 &= E^{+-+-} + E^{-+-+}, & E^8 &= E^{+--+} + E^{-+++}. \end{aligned}$$

In addition to the intra-layer exchange interactions, we calculated the inter-layer nearest-neighbor exchange coupling to gauge the degree of magnetic isolation of each layer. By considering parallel and anti-parallel spin configurations between the layers in the $1 \times 1 \times 2$ super cell, we find

$$J_{\perp} = \frac{(E^{++} + E^{--}) - (E^{+-} + E^{-+})}{4 \cdot 2 \langle S \rangle^2}. \quad (6)$$

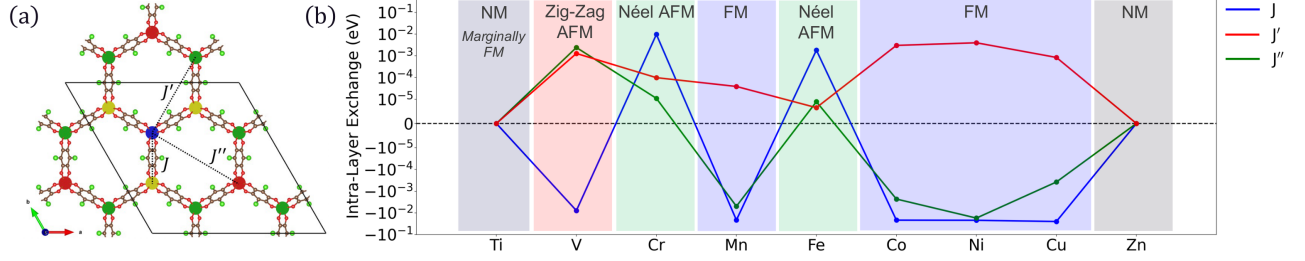


FIG. S1. (a) Schematic of the central magnetic ion (blue dot), nearest-neighbors (yellow dot), next-nearest-neighbors (green dot), and next-next-nearest-neighbors (red dot) J , J' , and J'' exchange parameters overlaid on the honeycomb lattice of transition-metal sites within a 2×2 super cell of the $[\text{M}_2\text{L}_3]^{2-}$ metal-organic framework. The black lines mark the unit cell. (b) Plot of exchange parameters in energy units as a function of transition-metal.

S2. DERIVATION OF MAGNON DISPERSION

The Dirac dispersion of magnons can be studied in a semi-classical magnon model. The effective spin interactions are described by the Heisenberg Hamiltonian $H = \sum_{\{i,j\}} J_{ij} \mathbf{S}_i \cdot \mathbf{S}_j$, where we include interactions on first nearest neighbor J , second nearest neighbor J' , and third nearest neighbor J'' .

A. The FM State

For ferromagnetic (FM) honeycomb lattice, we assign A and B spins for each unit cell (see Fig. S2 for il-

lustration) and use the Holstein-Primakoff representation of the spin operators in terms of the boson operators. In the reciprocal lattice where the boson operators are defined as $a_{\mathbf{k}} = \frac{1}{\sqrt{N/2}} \sum_{i \in A} e^{-i\mathbf{k} \cdot \mathbf{r}_i} a_i$ and $b_{\mathbf{k}} = \frac{1}{\sqrt{N/2}} \sum_{i \in B} e^{-i\mathbf{k} \cdot \mathbf{r}_i} b_i$, the Hamiltonian in the basis of $\Phi_{\mathbf{k}}^\dagger = (a_{\mathbf{k}}^\dagger, b_{\mathbf{k}}^\dagger)$ reads

$$H_{\text{FM}}(\mathbf{k}) = S \sum_{\mathbf{k}} \Phi_{\mathbf{k}}^\dagger \begin{bmatrix} \gamma_{\mathbf{k}}^{(2)} J' - 3J - 6J' - 3J'' & J\gamma_{\mathbf{k}}^{(1)*} + J''\gamma_{\mathbf{k}}^{(3)*} \\ J\gamma_{\mathbf{k}}^{(1)} + J''\gamma_{\mathbf{k}}^{(3)} & \gamma_{\mathbf{k}}^{(2)} J' - 3J - 6J' - 3J'' \end{bmatrix} \Phi_{\mathbf{k}} \quad (7)$$

where $\gamma_{\mathbf{k}}^{(n)} = \sum_{\delta \in \delta^{(n)}} e^{-i\mathbf{k} \cdot \delta}$ and $\delta^{(n)}$ refers to the n th nearest neighboring vectors, as defined in Fig. S2. The eigenvalues give the energy dispersion of the magnons as $\varepsilon_{\text{FM}}^\pm(\mathbf{k}) = S(\gamma_{\mathbf{k}}^{(2)} J' - 3J - 6J' - 3J'') \pm S|J\gamma_{\mathbf{k}}^{(1)} + J''\gamma_{\mathbf{k}}^{(3)}|$. This leads to the band degeneracy at the \mathbf{K}

points. Notice that other \mathbf{K} points are equivalent because of translational invariance, we only consider the two $\mathbf{K} = (0, \pm \frac{4\pi}{3\sqrt{3}})$ in the Cartesian coordinates. We can expand $\varepsilon_{\text{FM}}^\pm(\mathbf{k})$ near the two \mathbf{K} points,

$$\varepsilon_{\text{FM}}^\pm(\mathbf{K} + d\mathbf{k}) = S(\gamma_{(dk_x, \pm \frac{4\pi}{3\sqrt{3}} + dk_y)}^{(2)} J' - 3J - 6J' - 3J'') \pm S|J\gamma_{(dk_x, \pm \frac{4\pi}{3\sqrt{3}} + dk_y)}^{(1)} + J''\gamma_{(dk_x, \pm \frac{4\pi}{3\sqrt{3}} + dk_y)}^{(3)}| \quad (8)$$

where $d\mathbf{k} = (dk_x, dk_y)$. Expanding $\gamma_{\mathbf{k}}^{(n)} = \sum_{\delta \in \delta^{(n)}} e^{-i\mathbf{k} \cdot \delta}$ to the second order of $d\mathbf{k}$, we obtain the dispersion around the \mathbf{K} points as $\varepsilon_{\text{FM}}^\pm(\mathbf{K} + d\mathbf{k}) = -S(3J + 9J' + 3J'') \pm S(\frac{3}{2}J - 3J'')|d\mathbf{k}| + \frac{9}{4}SJ'|d\mathbf{k}|^2 + O(|d\mathbf{k}|^3)$.

The dispersion has a linear relation except for $J = 2J''$

and the energy of magnons at these points is $\varepsilon_{\text{FM}}^\pm(\mathbf{K}) = -S(3J + 9J' + 3J'')$. For the Heisenberg exchange parameters of the FM materials that we obtain, the dispersion always show linear dependence.

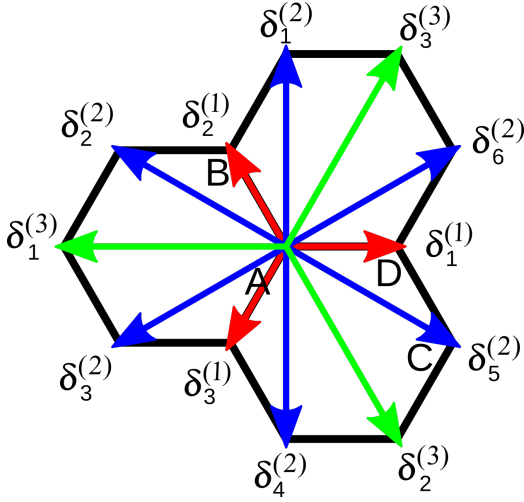


FIG. S2. Schematics of the honeycomb lattice with sub-lattice sites labelled as A , B , C , D , and vectors connecting first (red color), second (blue color), and third (green color) nearest neighbor.

B. The Néel AFM State

The Néel antiferromagnetic (AFM) state has two opposite spins in a unit cell, which we assign as A and B

spins. The Holstein-Primakoff transformations for A and B spins are

$$\begin{aligned}
 i \in A \\
 S_i^+ &= \sqrt{2S - a_i^\dagger a_i} a_i \\
 S_i^- &= a_i^\dagger \sqrt{2S - a_i^\dagger a_i} \\
 S_i^z &= S - a_i^\dagger a_i
 \end{aligned} \tag{9}$$

$$\begin{aligned}
 i \in B \\
 S_i^+ &= b_i^\dagger \sqrt{2S - b_i^\dagger b_i} \\
 S_i^- &= \sqrt{2S - b_i^\dagger b_i} b_i \\
 S_i^z &= -S + b_i^\dagger b_i
 \end{aligned}$$

where we assign boson operator a_i^\dagger (b_i^\dagger) for A (B) spins. Applying Fourier transformation to the momentum space, the Néel AFM Heisenberg Hamiltonian becomes $H_{\text{Néel}}(\mathbf{k}) = S \sum_{\mathbf{k}} \Psi_{\mathbf{k}}^\dagger [H_{\text{Néel}}]_{\mathbf{k}} \Psi_{\mathbf{k}}$ in the basis of $\Psi_{\mathbf{k}}^\dagger = (a_{\mathbf{k}}, b_{-\mathbf{k}}^\dagger)$, where $[H_{\text{Néel}}]_{\mathbf{k}}$ is a 2×2 matrix given in Eq. 10.

$$H_{\text{Néel}}(\mathbf{k}) = S \sum_{\mathbf{k}} \Psi_{\mathbf{k}}^\dagger \begin{bmatrix} \gamma_{\mathbf{k}}^{(2)} J' + 3J - 6J' + 3J'' & J\gamma_{\mathbf{k}}^{(1)} + J''\gamma_{\mathbf{k}}^{(3)} \\ J\gamma_{\mathbf{k}}^{(1)*} + J''\gamma_{\mathbf{k}}^{(3)*} & \gamma_{\mathbf{k}}^{(2)} J' + 3J - 6J' + 3J'' \end{bmatrix} \Psi_{\mathbf{k}} \tag{10}$$

To obtain the magnon dispersion, we use the Bogoliubov transformation

$$\begin{aligned}
 \alpha_{\mathbf{k}} &= u_{\mathbf{k}} a_{\mathbf{k}} - v_{\mathbf{k}} b_{-\mathbf{k}}^\dagger \\
 \beta_{\mathbf{k}} &= u_{\mathbf{k}} b_{-\mathbf{k}} - v_{\mathbf{k}} a_{\mathbf{k}}^\dagger
 \end{aligned} \tag{11}$$

where the quasi-particle excitations naturally obey bosonic commutation relation when $|u_{\mathbf{k}}|^2 - |v_{\mathbf{k}}|^2 = 1$ ($u_{\mathbf{k}}$ and $v_{\mathbf{k}}$ are complex coefficients to be determined). With the inverse transformation, the Hamiltonian can be written in terms of quasi-particles $\alpha_{\mathbf{k}}^\dagger$, $\alpha_{\mathbf{k}}$ and $\beta_{\mathbf{k}}^\dagger$, $\beta_{\mathbf{k}}$. To get rid of the off-diagonal terms in the Hamil-

tonian, we require $2(\gamma_{\mathbf{k}}^{(2)} J' + 3J - 6J' + 3J'')u_{\mathbf{k}}v_{\mathbf{k}} + (J\gamma_{\mathbf{k}}^{(1)} + J''\gamma_{\mathbf{k}}^{(3)})u_{\mathbf{k}}^2 + (J\gamma_{\mathbf{k}}^{(1)*} + J''\gamma_{\mathbf{k}}^{(3)*})v_{\mathbf{k}}^2 = 0$. Looking at the imaginary part of the equation, we can assume that $(J\gamma_{\mathbf{k}}^{(1)} + J''\gamma_{\mathbf{k}}^{(3)})$, $u_{\mathbf{k}}$, $v_{\mathbf{k}}$ has the following form

$$\begin{aligned}
 J\gamma_{\mathbf{k}}^{(1)} + J''\gamma_{\mathbf{k}}^{(3)} &= \left| J\gamma_{\mathbf{k}}^{(1)} + J''\gamma_{\mathbf{k}}^{(3)} \right| e^{i\eta} \\
 u_{\mathbf{k}} &= |u_{\mathbf{k}}| e^{i(\eta/2 + \pi)} \\
 v_{\mathbf{k}} &= |v_{\mathbf{k}}| e^{-i\eta/2}
 \end{aligned} \tag{12}$$

where η is a phase parameter that can be calculated from the first equation in Eq. 12. Thus, we can obtain the magnon energy dispersion as well as the dispersion near the Γ point,

$$\varepsilon_{\text{Néel}}(\mathbf{k}) = S \sqrt{(\gamma_{\mathbf{k}}^{(2)} J' + 3J - 6J' + 3J'')^2 - |J\gamma_{\mathbf{k}}^{(1)} + J''\gamma_{\mathbf{k}}^{(3)}|^2} \tag{13}$$

$$\varepsilon_{\text{Néel}}(d\mathbf{k}) = S \sqrt{(\gamma_{d\mathbf{k}}^{(2)} J' + 3J - 6J' + 3J'')^2 - |J\gamma_{d\mathbf{k}}^{(1)} + J''\gamma_{d\mathbf{k}}^{(3)}|^2} \tag{14}$$

where $d\mathbf{k} = (dk_x, dk_y)$. Expanding $\gamma_{\mathbf{k}}^{(n)} = \sum_{\delta \in \delta^{(n)}} e^{-i\mathbf{k} \cdot \delta}$ to the linear order of $d\mathbf{k}$, we obtain the linear dispersion around the Γ points as $\varepsilon_{\text{Néel}}(d\mathbf{k}) = S\nu|d\mathbf{k}| + O(|d\mathbf{k}|^2)$, where $\nu = \sqrt{\frac{9}{2}J^2 + \frac{45}{2}JJ'' + 18J''^2 - 27J'(J + J')}$ is non-zero for the parameters of the Néel AFM materials that we obtain.

C. The Zig-zag AFM State

For the zig-zag AFM honeycomb lattice we assign A , B , C , and D spins in an enlarged 2×2 unit cell with A and B spins pointing up while C and D spins pointing down as shown in Fig. S2. Similar to the Holstein-Primakoff transformation for Néel AFM state, we can find the Heisenberg Hamiltonian in the basis of $\Lambda_{\mathbf{k}}^\dagger = (a_{\mathbf{k}}, b_{\mathbf{k}}, c_{-\mathbf{k}}^\dagger, d_{-\mathbf{k}}^\dagger)$

$$H_{\text{zig-zag}}(\mathbf{k}) = S \sum_{\mathbf{k}} \Lambda_{\mathbf{k}}^\dagger [H_{\text{zig-zag}}]_{\mathbf{k}} \Lambda_{\mathbf{k}} \quad (15)$$

$$[H_{\text{zig-zag}}]_{\mathbf{k}} = \begin{bmatrix} \chi_1 & \phi_1^* & \chi_2 & \phi_2 \\ \phi_1 & \chi_1 & \phi_2^* & \chi_2 \\ \chi_2 & \phi_2 & \chi_1 & \phi_1^* \\ \phi_2^* & \chi_2 & \phi_1 & \chi_1 \end{bmatrix} \quad (16)$$

where we define matrix elements $\chi_1 = -J + [2 \cos(\sqrt{3}k_y) + 2]J' + 3J''$, $\chi_2 = [2 \cos(\frac{3}{2}k_x + \frac{\sqrt{3}}{2}k_y) + 2 \cos(\frac{3}{2}k_x - \frac{\sqrt{3}}{2}k_y)]J'$, $\phi_1 = (e^{-\frac{1}{2}k_x - \frac{\sqrt{3}}{2}k_y} + e^{-\frac{1}{2}k_x + \frac{\sqrt{3}}{2}k_y})J$, and $\phi_2 = e^{-k_x}J + (e^{2k_x} + e^{-k_x - \sqrt{3}k_y} + e^{-k_x + \sqrt{3}k_y})J''$. Here we separate $\mathbf{k} = (k_x, k_y)$ in Cartesian coordinates. Using the Bogoliubov transformation we can solve for the magnon energy dispersion

$$\varepsilon_{\text{zig-zag}}^\pm(\mathbf{k}) = S \sqrt{\chi_1^2 + |\phi_1|^2 - \chi_2^2 - |\phi_2|^2 \pm 2\sqrt{(\chi_1 \Im \phi_1 + \chi_2 \Im \phi_2)^2 + (\chi_1 \Re \phi_1 - \chi_2 \Re \phi_2)^2 - (\Im \phi_1 \Re \phi_2 + \Im \phi_2 \Re \phi_1)^2}}, \quad (17)$$

which leads to zero energies at Γ and M points for the

lower band and linear dispersion around them.

* laneca@lanl.gov

¹ H. Xiang, C. Lee, H.-J. Koo, X. Gong, and M.-H. Whangbo, Dalton Transactions **42**, 823 (2013).